

Surface engineering of RhOOH nanosheets promotes hydrogen evolution in alkaline



Shuxing Bai ^{a,1}, Miao Xie ^{b,1}, Tao Cheng ^{b,**}, Kailei Cao ^a, Yong Xu ^{b,***}, Xiaoqing Huang ^{a,*}

^a College of Chemistry, Chemical Engineering and Materials Science, Soochow University, Jiangsu, 215123, China

^b Institute of Functional Nano & Soft Materials (FUNSOM), Jiangsu Key Laboratory for Carbon-Based Functional Materials and Devices, Soochow University, Jiangsu, 215123, China

ARTICLE INFO

Keywords:

Rhodium
Rhodium oxyhydroxide
Nanosheet
Hydrogen evolution reaction
Alkaline electrolyte

ABSTRACT

Hydrogen evolution reaction (HER), a promising strategy for converting electricity to value-added H₂ fuel, is a key half reaction of the overall water splitting. However, HER is suffering from the sluggish kinetics in alkaline. We here demonstrate a highly efficient catalyst for alkaline HER via surface and interface engineering of RhOOH nanosheets (NSs). The surface structure of RhOOH NSs can be precisely tuned by altering the cyclic voltammogram cycles (CVs) in the activation process, leading to the formation of strongly synergized RhOOH/Rh interface for boosted HER activity in alkaline. The optimized catalyst exhibits a promising alkaline HER performance with overpotential of 18 mV at current density of 10 mA·cm⁻² and Tafel slope of 19.3 mV·dec⁻¹ in 1 M KOH, which surpasses the commercial Pt/C, Rh NSs/C and RhOOH NSs/C. Detailed experiments and theoretical calculations reveal that the synergy between RhOOH and Rh significantly promotes the H₂O adsorption/dissociation to form H_{ad} and the H_{ad} desorption to produce H₂.

1. Introduction

The electrochemical water (H₂O) splitting has recently attracted great attention for converting electricity to value-added fuel [1,2]. Generally, the overall H₂O splitting involves two critical half reactions, i.e., hydrogen evolution reaction (HER) and oxygen evolution reaction (OER), which are generally performed in acidic or alkaline condition [3–5]. Despite significant progress has been achieved on acidic HER and OER, the quest for robust catalysts is driven by the current disadvantages of poor stability of catalyst in acidic condition [6–10]. To this end, the design of efficient catalysts for alkaline H₂O splitting is thus of great importance. However, alkaline HER suffers from the sluggish kinetics for reducing H₂O to H₂, where the reaction rate in alkaline media is ~2–3 orders of magnitude lower than that of protons (H⁺) reduction to H₂ in acidic media [11,12].

In principle, HER process undergoes Volmer step to form adsorbed hydrogen (H_{ad}) and Heyrovsky/Tafel step to form H₂ [13–15]. Over the past decades, tremendous efforts have been devoted to designing catalysts for alkaline HER [16,17]. To improve the alkaline HER activity, the

ideal catalysts are required to overcome the sluggish kinetics of Volmer step and remain stable during the electrocatalysis. Therefore, great attention has been dedicated to the functionalization and modification of catalysts to improve their alkaline HER activity [16–20]. For instance, it is shown that Pt(111) modified by Ni(OH)₂ or Co(OH)₂ can improve the kinetics and activity of alkaline HER [18–20]. Some mechanisms including hydrogen binding energy theory [21,22], bifunctional mechanism [19], potential of zero free charge theory [23], and 2B theory [24], have been proposed for elucidating the enhanced HER activity. Despite great progress has been made, the design of efficient alkaline HER catalysts is facing great challenges.

Herein, we demonstrated a highly efficient catalyst for alkaline HER via surface engineering of RhOOH nanosheets (NSs). The surface structure of RhOOH NSs can be precisely tuned by altering the cyclic voltammogram cycles (CVs) in the activation process, leading to the formation of strongly synergized RhOOH/Rh interface for enhanced alkaline HER activity. The optimized RhOOH NSs/C after 40 CVs activation cycles in 1 M KOH (named as RhOOH NSs/C-OH-40) exhibited superior alkaline HER activity with an overpotential of 18 mV at a

* Corresponding author.

** Corresponding author.

*** Corresponding author.

E-mail addresses: tcheng@suda.edu.cn (T. Cheng), xuy@suda.edu.cn (Y. Xu), hxq006@suda.edu.cn (X. Huang).

¹ Shuxing Bai and Miao Xie contributed equally to this work.

current density of 10 mA cm^{-2} and a Tafel slope of 19.3 mV dec^{-1} in 1 M KOH , which outperforms the commercial Pt/C, Rh NSs/C and RhOOH NSs/C under the same conditions. Detailed experiments and density functional theory (DFT) calculations revealed that the synergy between RhOOH and Rh at RhOOH/Rh interface significantly promoted H_2O dissociation and the desorption of H_{ad} to H_2 , leading to a high alkaline HER activity.

2. Experimental section

2.1. Synthesis of Rh NSs

8.0 mg rhodium (III) acetylacetone ($\text{Rh}(\text{acac})_3$, J&K), 3.0 mL formaldehyde solution (36.5–38.0%, Sigma), 1 mL diphenyl ether (Aladdin) and 2 mL oleylamine (J&K) were mixed into a bottle (15 mL). After ultrasonication for 30 min, the resulting mixture was transferred into a Teflon inlet of stainless autoclave and heated to 180°C in an oven and maintained at the same temperature for 5 h. After cooling to room temperature, the colloidal products were collected and washed by cyclohexane/acetone with ratio of 2:8 three times via centrifugation.

2.2. Preparations of supported catalysts

Rh NSs, carbon (C, Vulcan XC72R), and cyclohexane (5 mL) were mixed with in a glass vial (35 mL). After ultrasonication for 10 min, 10 mL ethanol was added into the mixture, followed by additional 20 min ultrasonication. The products were centrifugated and washed with acetone, and then dried at 60°C overnight in an oven. The products were finally subjected to thermal annealing at 250°C for 1 h in air to obtain the RhOOH NSs/C and in H_2/Ar (5 vol%) at 250°C for 1 h to obtain Rh NSs/C.

2.3. Characterizations

The morphology was determined by transmission electron microscopy (TEM, Hitachi, HT7700, 120 kV), high-resolution TEM (HRTEM, a FEI Tecnai F20 transmission electron microscope, 200 kV), spherical aberration TEM (SATEM, Titan Cubed Themis G2 300, 300 kV), and atomic force microscopy (AFM, Multimode 8). X-ray diffraction (XRD) patterns were collected using an X'Pert-Pro X-ray powder diffractometer equipped with a Cu radiation source ($\lambda = 0.15406 \text{ nm}$). Thermogravimetric analysis (TGA) measurements were performed on a thermogravimetric analyzer (SII TG/DTA 6300) at 25 – 800°C with a heating rate of $10^\circ\text{C min}^{-1}$ under flowing air. H_2 -temperature programmed reduction (TPR) measurements were performed on FINESORB-3010. Typically, 10 mg sample was fixed in an U-shape quartz tube, followed by treated with H_2/Ar (5%) with a heating rate of $10^\circ\text{C min}^{-1}$. The temperature and current of thermal conductivity detector were 60°C and 45 mA , respectively. The surface analysis was determined by X-ray photoelectron spectroscopy (XPS, Thermo Scientific, ESCALAB 250 XI). Rh loadings were determined by the inductively coupled plasma atomic emission spectroscopy (ICP-AES, 710-ES, Varian).

2.4. Electrochemical measurements

Electrochemical measurements were performed in a three-electrode cell by using CHI660 electrochemical workstation (Chenhua, Shanghai). A saturated calomel electrode (SCE) and a carbon electrode were used as the reference and counter electrodes, respectively. The working electrode was composed by casting of catalyst onto a glassy-carbon electrode (GCE, diameter: 5 mm, area: 0.196 cm^2). The catalyst ink was prepared by ultrasonically mixing catalysts with $500 \mu\text{L}$ isopropanol, and $10 \mu\text{L}$ 5 wt% Nafion solutions for 1 h. The actual mass concentrations of the Rh species in all catalyst inks were controlled at $0.25 \text{ mg}_{\text{Rh}} \cdot \text{mL}^{-1}$. Then, the inks ($10 \mu\text{L}$) were deposited onto a GCE dried at room temperature, to serve as the working electrodes. HER measurements were conducted in

1 M KOH , 0.1 M KOH , $0.05 \text{ M H}_2\text{SO}_4$ and $0.5 \text{ M H}_2\text{SO}_4$. All the fresh electrolytes with required concentrations were prepared in a volumetric flask by dissolving the required amount of KOH or H_2SO_4 in Milli-Q water and purged with N_2 before the measurement. CVs were performed at the scan rate of 50 mV s^{-1} between 0.05 and 1.25 V vs. standard hydrogen electrode (V_{RHE}) in 1 M KOH . The catalysts were cycled with different cycles (0–50) at the scan rate of 200 mV s^{-1} between 0.05 and $1.25 \text{ V}_{\text{RHE}}$ in 1 M KOH or 0.1 M HClO_4 before linear sweep voltammetry test. Linear sweep voltammetry was carried out between -0.1 and $0.15 \text{ V}_{\text{RHE}}$ at the scan rate of 5 mV s^{-1} with 95% insulation resistance compensation for activity tests. Electrochemical impedance spectroscopies (EIS) were measured with frequencies ranging from 100 kHz to 0.1 Hz and peak-to-peak amplitude of 5 mV with 2000 revolutions per minute. The chronopotentiometry was measured under a constant current density of 10 mA cm^{-2} for stability test. The detailed processes of CO stripping experiments were listed as follows: First, RhOOH NSs/C was activated with different CV activation cycles (0–50) at the scan rate of 200 mV s^{-1} between 0.05 and $1.25 \text{ V}_{\text{RHE}}$ in 1 M KOH for obtaining RhOOH NSs/C-OH-x; Second, CO adsorption saturation on the RhOOH NSs/C-OH-x was implemented by continuous CO flow for 0.5 h in 1 M KOH ; Finally, CO stripping experiments were performed at the scan rate of 50 mV s^{-1} between 0.05 and $1.25 \text{ V}_{\text{RHE}}$ in 1 M KOH . All electrochemical measurements were performed at room temperature.

2.5. Computational details

The quantum mechanics (QM) calculations were carried out using the VASP software, version 5.4.4 [25–27]. We used the Perdew, Burke, and Ernzerhof (PBE) flavor [28] of DFT with the post-stage DFT-D3 method to correct for London dispersion (van der Waals attraction) with Becke-Johnson damping [29]. The projector augmented wave (PAW) method was used to account for core-valence interactions [30,31]. The kinetic energy cutoff for plane wave expansions was set to 400 eV , and reciprocal space was sampled by the Γ -centered Monkhorst-Pack scheme with a grid of $3 \times 3 \times 1$. The vacuum layer is at least 15 \AA above the surface. The convergence criteria are $1 \times 10^{-7} \text{ eV}$ energy differences for solving the electronic wave function. The Methfessel-Paxton smearing of second order with a width of 0.1 eV was applied. All atomic coordinates were converged to within $1 \times 10^{-2} \text{ eV \AA}^{-1}$ for maximal components of forces.

In this work, all free energies were calculated as

$$G_{298.15K} = E_{\text{elec}}^{\text{solv}} + E_{\text{ZPVE}} - \sum_{\tilde{v}} \frac{hv}{e^{hv/kT} - 1} - T \times S_m^v$$

The vibrational frequencies were evaluated for only surface adsorbates and were calculated. According to the calculated frequency results, we obtain the zero-point vibrational energy (ZPVE) and adsorption entropy S_m^v .

$$S_m^v = \sum_{\tilde{v}} R \left\{ \frac{\beta hc\tilde{v}}{e^{\beta hc\tilde{v}} - 1} - \ln(1 - e^{-\beta hc\tilde{v}}) \right\}$$

Where R is gas constant, β is $1/T^*k_b$ (k_b is Boltzman constant), h is Plank constant, c is light speed, and v is wave number.

We carried out simulations for three systems, including Pt(111), Rh (111), and Rh (111)-Rh-O interface (to mimic the RhOOH/Rh interface). The Pt(111) and Rh(111) surface was modeled by a 3×3 unit cell with four periodic atom layers, and a vacuum thickness of 15 \AA was used to remove any interactions between slabs. Furthermore, One Rh atoms on the top layer of the Rh(111) system were replaced by O atoms for Rh (111)-Rh-O interface system under the same conditions. Two water molecules were placed on the surface to simulate the hydrogen evolution reaction. During the geometry optimizations, the atoms in the bottom two layer were fixed at their bulk positions, whereas the rest of

atoms were allowed to relax. The adsorption energies (E_{ads}) for the H atom were calculated according to

$$\Delta G_{ads} = G_{H\text{-surface}} - G_{\text{Surface}} - \frac{1}{2}G_{H_2}$$

Where $\Delta G_{H\text{-surface}}$, G_{Surface} , and G_{H_2} represent the free energies of the corresponding surface (clean Pt (111), Rh (111) surface, or the RhOOH/Rh interface), surface, and H_2 in gas phase, respectively. In the calculation of adsorption energies, we have considered top site, bridge site, and two hollow sites (*hpc* and *fcc*), and reported the lowest one in the manuscript. The calculated results show that the most stable site of H atom in all systems is *fcc* site.

3. Results and discussion

Rh NSs were prepared by reducing $\text{Rh}(\text{acac})_3$ with diphenyl ether/

oleylamine in the presence of formaldehyde. TEM and SEM measurement was employed to characterize the morphology, as displayed in Fig. 1a–c. It was shown that the products with the shape of two-dimensional sheet gave a mean thickness of ~1.8 nm (Fig. 1d). Afterwards, the as-prepared NSs were loaded on C with a loading amount of 20 wt%, followed by calcination at 250 °C in air for 1 h to generate RhOOH NSs/C (Fig. S1a–b) or in H_2/Ar (5 vol%) for 1 h to obtain Rh NSs/C (Fig. S1c–d). The crystalline structures of the supported catalysts were determined by XRD and HRTEM measurements. As shown in Fig. 1e, the characteristic peaks in the XRD pattern of RhOOH NSs/C were indexed as RhOOH orthorhombic phase (PDF No. 27–1383) [32], while those peaks in the XRD pattern of Rh NSs/C were ascribed to the face-centered cube (*fcc*) phase of metallic Rh (PDF No. 05–0685) [33]. The HRTEM images lattice distances of 0.223 and 0.216 nm in the HRTEM images can be ascribed to the (111) facet of RhOOH and the (111) facet of *fcc* phase Rh, respectively (Fig. 1f–g) [32,33]. The TGA

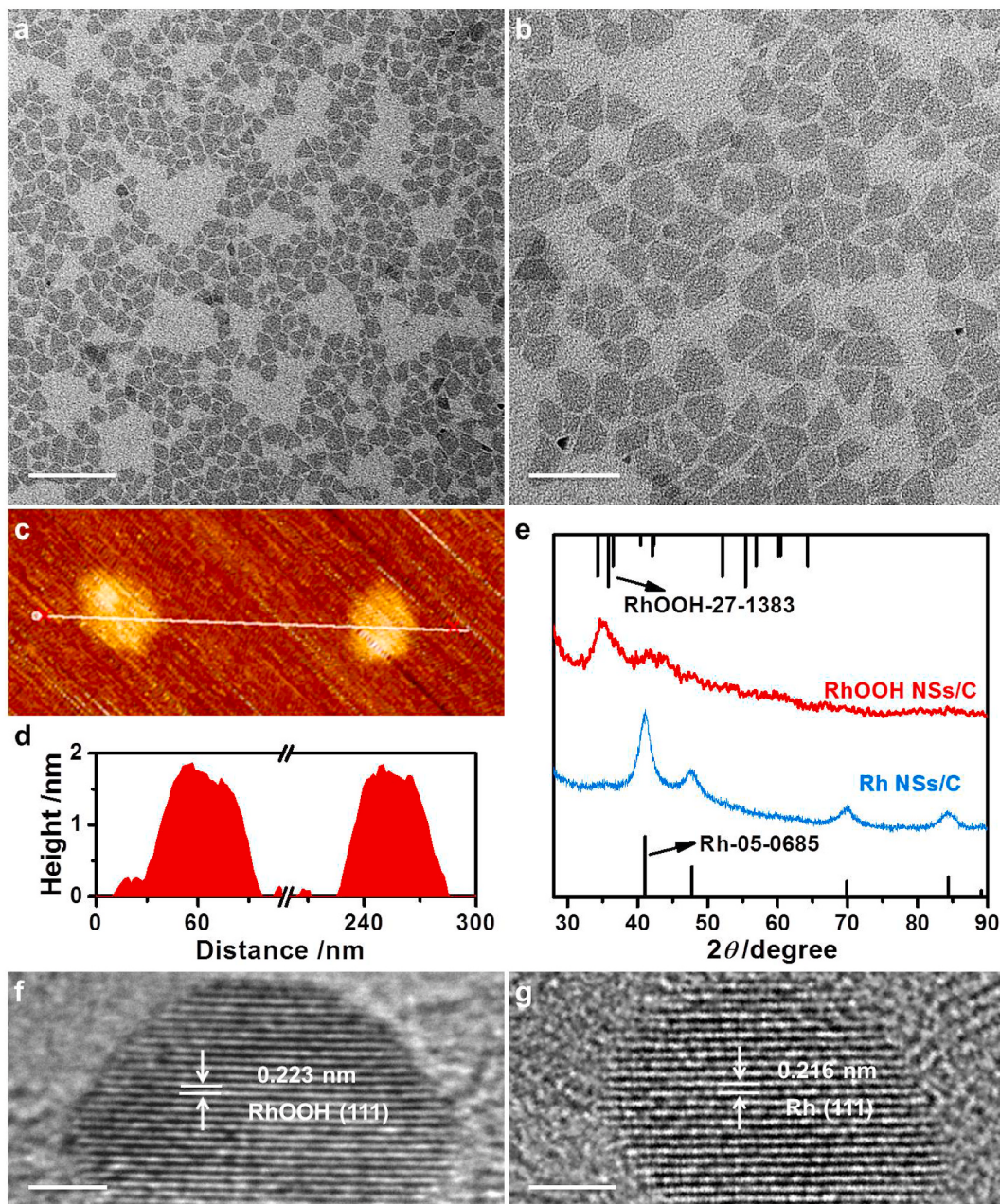


Fig. 1. (a, b) TEM images, (c) AFM image and (d) corresponding height profiles of Rh NSs. (e) XRD patterns of RhOOH NSs/C and Rh NSs/C. HRTEM images of (f) RhOOH NSs/C and (g) Rh NSs/C. The scale bars in (a), (b), (f) and (g) are 100, 50, 2, and 2 nm, respectively.

measurements were carried out to better understand the formation mechanism of RhOOH. The TGA curve of Rh NSs/C-initial under flowing air (Fig. S2a, black curve) displayed two apparent weight losses. The weight loss at 150–250 °C (~5.5%) was attributed to the removal of surface species which were introduced in the synthesis and washing process, and the significant weight loss at 300–600 °C was ascribed to the combustion of carbon support. Moreover, TGA measurement was performed for Rh NSs without carbon support (Fig. S2a, red curve). Considering that the removal of surface species would lead to the weight loss at 50–250 °C (black curve in Fig. S2a), the slight weight increase at this temperature range should be caused by the formation of RhOOH (Fig. S2a, red curve). Another weight increase at 450–600 °C was attributed to the formation of Rh₂O₃ (Fig. S2a, red curve). To further confirm the above conclusion, XRD measurement was performed for Rh NSs/C after calcination in air at 450 °C (Rh NSs/C-A-450) and 600 °C (Rh NSs/C-A-600). As shown in Fig. S2b, Rh (PDF No. 05-0685) and Rh₂O₃ (PDF No. 71-0674) were identified in the XRD patterns of Rh NSs/C-A-450 and Rh NSs/C-A-600, respectively, which indicated that the oxidation of Rh into Rh₂O₃ occurred at temperature over than 450

°C. Therefore, the evolution of species during the calcination process should be as follows: 1) the removal of residual surface species of Rh NSs; 2) the formation of RhOOH with the assistance of surface species (formaldehyde, H₂O, etc.); 3) RhOOH decomposition [34]; 4) complete oxidation to form Rh₂O₃.

Electrochemical tests were performed in N₂-saturated electrolyte at room temperature using a standard three electrodes system, and the commercial Pt/C (20 wt%, Johnson-Matthey) was used as a reference. The calibration of SCE was performed before electrochemical tests (Fig. S3). Afterwards, the catalysts were scanned at a sweep rate of 200 mV s⁻¹ for 40 cycles in 1 M KOH with CV activation, which were recorded as RhOOH NSs/C-OH-40, Rh NSs/C-OH-40 and Pt/C-OH-40, respectively. TEM image displayed that no obvious morphology changes were observed in RhOOH NSs/C-OH-40 after CV activation (Fig. S4). The hydrogen desorption (H_{upd}) peaks of these catalysts in CV curves at a sweep rate of 50 mV s⁻¹ were used to study the amount of surface metal atoms. As shown in Fig. 2a, the electrochemical specific surface areas (ECSAs) devoted by metallic state atoms of RhOOH NSs/C-OH-40, Rh NSs/C-OH-40 and Pt/C-OH-40 in 1 M KOH were 26.3, 104.5, and

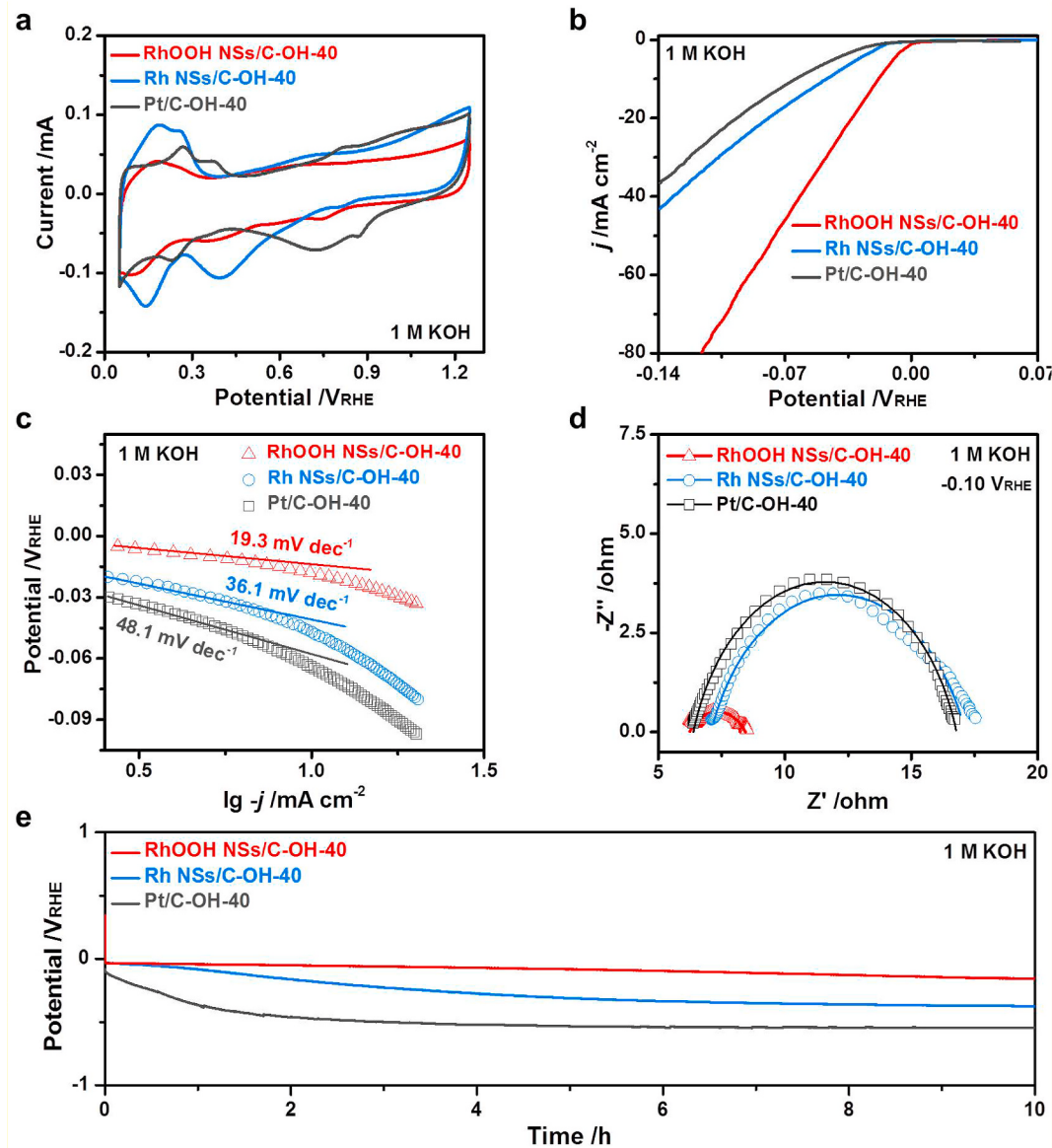


Fig. 2. Alkaline HER performance on RhOOH NSs/C-OH-40, Rh NSs/C-OH-40, and Pt/C-OH-40. (a) Cyclic voltammogram curves, (b) polarization curves, (c) Tafel slopes, (d) Nyquist plots at -0.10 V_{RHE}, and (e) chronopotentiometry curves at 10 mA•cm⁻² in 1 M KOH.

$63.8 \text{ m}^2 \text{ g}^{-1}$, respectively (determined by H_{upd} at 0.05–0.45 V_{RHE}). The above results implied that RhOOH was partially converted to Rh after CV activation, which was further verified by the appearance of Rh characteristic peaks in XRD patterns (Fig. S5). Fig. 2b displayed the polarization curves of RhOOH NSs/C-OH-40, Rh NSs/C-OH-40, and Pt/C-OH-40 in 1 M KOH with a sweep rate of 5 mV s⁻¹ and 95% insulation resistance compensation. It was found that RhOOH NSs/C-OH-40 exhibited the highest HER activity in comparison to Rh NSs/C-OH-40 and Pt/C-OH-40 (Fig. 2b). To quantitatively compare the HER activity, the overpotentials at a current density of 10 mA cm⁻² and the current densities at 0.07 V_{RHE} in 1 M KOH were summarized in Fig. S6. Specifically, the current density of RhOOH NSs/C-OH-40 at 0.07 V_{RHE} was 42.9 mA cm⁻², which was 2.4 and 3.7 times higher than that of Rh NSs/C-OH-40 (18.0 mA cm⁻²) and Pt/C-OH-40 (11.5 mA cm⁻²) (Fig. S6a). Moreover, the overpotential of RhOOH NSs/C-OH-40 (18 mV) was much lower than that of Rh NSs/C-OH-40 (46 mV) and Pt/C-OH-40 (65 mV) (Fig. S6b). On the other hand, the Tafel slopes of the Rh NSs/C-OH-40 and Pt/C-OH-40 were 36.1 and 48.1 mV·dec⁻¹, respectively, indicating that the adsorption and dissociation of H₂O to form H_{ad} via Volmer reaction was the rate-determining step (Fig. 2c) [35]. By contrast, RhOOH NSs/C-OH-40 exhibited a much lower Tafel slope of 19.3 mV·dec⁻¹ than that of Rh NSs/C-OH-40 and Pt/C-OH-40. Furthermore, EIS was used to gain insight into the electron transport capability and the kinetics of catalysts during HER test. As shown in Fig. 2d&Fig. S7, the Nyquist plots of three catalysts were fitted using the equivalent electric circuit [17], where the charge transfer resistance (Rct) was inversely proportional to the rate of hydrogen adsorption (Volmer step, H₂O + e⁻ = H_{ads} + OH⁻) [23]. It was turned out that the Rct of RhOOH NSs/C-OH-40 ($2.3 \pm 0.3 \Omega \text{ cm}^2$) was obviously smaller than that of Rh NSs/C-OH-40 ($7.9 \pm 3.8 \Omega \text{ cm}^2$) and Pt/C-OH-40 ($8.4 \pm 4.2 \Omega \text{ cm}^2$), indicating that charge transfer and kinetics of Volmer step were greatly promoted on RhOOH NSs/C-OH-40 (Fig. S7d). Interestingly, different from the Rct of Rh NSs/C-OH-40 and Pt/C-OH-40 that increased with the potential, the invariable Rct at different potentials on RhOOH NSs/C-OH-40 suggested that the enhanced electron transfer favors H₂ evolution over RhOOH NSs/C-OH-40, leading to the decrease of Tafel slope (Fig. S7d) [23]. In addition, we performed the chronopotentiometry at 10 mA cm⁻² for durability test. Compared to Rh NSs/C-OH and Pt/C-OH-40, RhOOH NSs/C-OH-40 exhibited an obviously better durability in 10 h (Fig. 2e). Both the morphology and structure were reserved in the used RhOOH NSs/C-OH-40 (Fig. S8), while obvious sintering occurs in the used commercial Pt/C (Fig. S9), indicating that RhOOH NSs/C-OH-40 can be used as a highly efficient catalyst for alkaline HER. It should be noted that the current alkaline HER performance on RhOOH NSs/C-OH-40 outperformed many reported catalysts in literature reports (Table S1).

To further highlight the HER performance, RhOOH NSs/C-OH-40 was tested under different conditions. It was shown that the decrease of KOH concentration led to a decay in HER activity (Fig. S10). The current density of RhOOH NSs/C-OH-40 at 0.07 V_{RHE} decreased from 42.9 to 26.3 mA cm⁻² when the KOH concentration was decreased from 1 to 0.1 M (Fig. S10c). Similar trends were observed on Rh NSs/C-OH-40 and Pt/C-OH-40. Specifically, the Tafel slopes of RhOOH NSs/C-OH-40, Rh NSs/C-OH-40 and Pt/C-OH-40 in 0.1 M KOH were 28.9, 55.8 and 123.6 mV·dec⁻¹, respectively (Fig. S10d). Furthermore, HER was performed in acidic solution (0.5 and 0.05 M H₂SO₄), as represented in Fig. S11. Different from the variable HER performance under alkaline condition, all the catalysts (*i.e.*, RhOOH NSs/C-OH-40, Rh NSs/C-OH-40 and Pt/C-OH-40) presented similar current densities at 0.07 V_{RHE} and Tafel slopes in 0.05 M H₂SO₄. For instance, the current densities at 0.07 V_{RHE} were 28.1, 28.3 and 26.2 mA cm⁻², while the Tafel slopes were 24.9, 17.8 and 16.6 mV·dec⁻¹ on RhOOH NSs/C-OH-40, Rh NSs/C-OH-40 and Pt/C-OH-40, respectively (Figs. S11b–c). Further increase of the H₂SO₄ concentration from 0.05 to 0.5 M led to an increase of current density at 0.07 V_{RHE} and a decrease of Tafel slope. Specifically, the current density at 0.07 V_{RHE} was 28.1 mA cm⁻² in 0.05 M H₂SO₄ on

RhOOH NSs/C-OH-40, which further increased to 97.9 mA cm⁻² in 0.5 M H₂SO₄ (Fig. S11e). Correspondingly, the Tafel slope decreased from 24.9 to 12.5 mV·dec⁻¹ when H₂SO₄ concentration was increased from 0.05 to 0.5 M. Similar trends were observed on Rh NSs/C-OH-40 and Pt/C-OH-40 under the same conditions. However, different from the superior HER performance in KOH, RhOOH NSs/C-OH-40 displayed a much poorer acidic HER performance comparing with Rh NSs/C-OH-40 and Pt/C-OH-40 in H₂SO₄ with high concentration (Figs. S11e–f). The deterioration of HER performance in H₂SO₄ with high concentration over RhOOH NSs/C-OH-40 might be attributed to the consumption of surface RhOOH by H₂SO₄ which severely damages the strong synergy between RhOOH and Rh.

The above results vividly demonstrated that strongly synergized RhOOH/Rh interface, which was *in situ* formed during the activation process, can significantly boost the alkaline HER performance. To further investigate mechanism, RhOOH NSs/C was pre-activated for different CV activation cycles before HER test. As shown in Fig. 3a, the increase of activation cycles led to the increase in alkaline HER activity. Typically, the overpotential of RhOOH NSs/C-initial (without activation) at 10 mA cm⁻² was 88 mV, which significantly decreased to 18 mV after 40 CV activation cycles (RhOOH NSs/C-OH-40). Correspondingly, the current densities of RhOOH NSs/C-initial at 0.07 V_{RHE} was 7.5 mA cm⁻², which gradually increased to 42.9 mA cm⁻² as increasing the CV activation cycles to 40 (Table S2). Meanwhile, the Tafel slope decreased from 75.4 mV·dec⁻¹ for RhOOH NSs/C-initial to 19.3 mV·dec⁻¹ for RhOOH NSs/C-OH-40 (Fig. S12a). Further increase of the CV activation cycles to 50 led to slight influence on the HER activity. Specifically, when RhOOH NSs/C-OH-50 was used as catalyst in 1 M KOH, the overpotential, current density at 0.07 V_{RHE} and Tafel slope were 22 mV, 42.4 mA cm⁻² and 18.0 mV·dec⁻¹, respectively (Table S2). In addition, the increase of CV activation cycles slightly influenced the Nyquist plots (Fig. S12b), indicating that the promoted electron transfer and hydrogen evolution played a vital role in the enhancement on alkaline HER activity. Furthermore, CO stripping experiments were performed to reveal the mechanism, as demonstrated in Fig. 3b and Table S3. The appearance of CO stripping peaks suggests that RhOOH was converted into metallic Rh after activation. The different areas of curves indicated that the ratios of metallic Rh were variable in RhOOH NSs after different CV activation cycles, which further confirmed the existence of strong synergy between RhOOH and Rh at interface. On the other hand, CO stripping process was employed to investigate the generation of OH_{ad}, in which the onset potential of CO stripping peak can be used to evaluate the binding energy of OH_{ad} [36]. The onset potentials of CO stripping peak remained at 0.56 V_{RHE} when the CV activation cycles were increased from 0 to 40, which positively shifted to 0.58 V_{RHE} when the CV activation cycles were further increased to 50 (Fig. 3b and Table S3), suggesting that excess metallic Rh species on the surface of catalyst can suppress the formation of OH_{ad}, leading to the decay in HER activity. In contrast, the effect of CV activation cycles in 1 M KOH for Pt/C on alkaline HER performance was further investigated. As depicted in Fig. S13a, it was found that the increase of CV activation cycles resulted in the decrease of alkaline HER activity on Pt/C. Typically, the overpotential of Pt/C-initial at 10 mA cm⁻² was 50 mV, which significantly increased to 67 mV after 50 CV activation cycles (Pt/C-OH-50). Meanwhile, the Tafel slope increased from 39.2 mV·dec⁻¹ for Pt/C-initial to 48.1 mV·dec⁻¹ for Pt/C-OH-50 (Fig. S13b).

XPS measurement was employed to analyze the surface species at strongly synergized RhOOH/Rh interface. As shown in Fig. 3c, S14 and S15a, the peaks at 307.5 and 312.2 eV corresponded to Rh⁰ 3d_{5/2} and Rh⁰ 3d_{3/2}, while the peaks at 308.5 and 313.5 eV were indexed as Rh³⁺ 3d_{5/2} and Rh³⁺ 3d_{3/2}, respectively [37–39]. O 1s XPS and H₂-TPR of RhOOH NSs/C and commercial Rh₂O₃ (Rh₂O₃-com, Yuanye Biotechnology Co., Ltd) were used to further confirm the formation of RhOOH. As shown in Fig. S15b, the peaks at 535.9, 533.3, 532.7 and 531.0 eV in O 1s XPS curve of RhOOH NSs/C corresponded to the chemisorbed oxygen (O_{ad}), Rh-OH, carbonate like species (C-O), and O species (O_{ox}) in

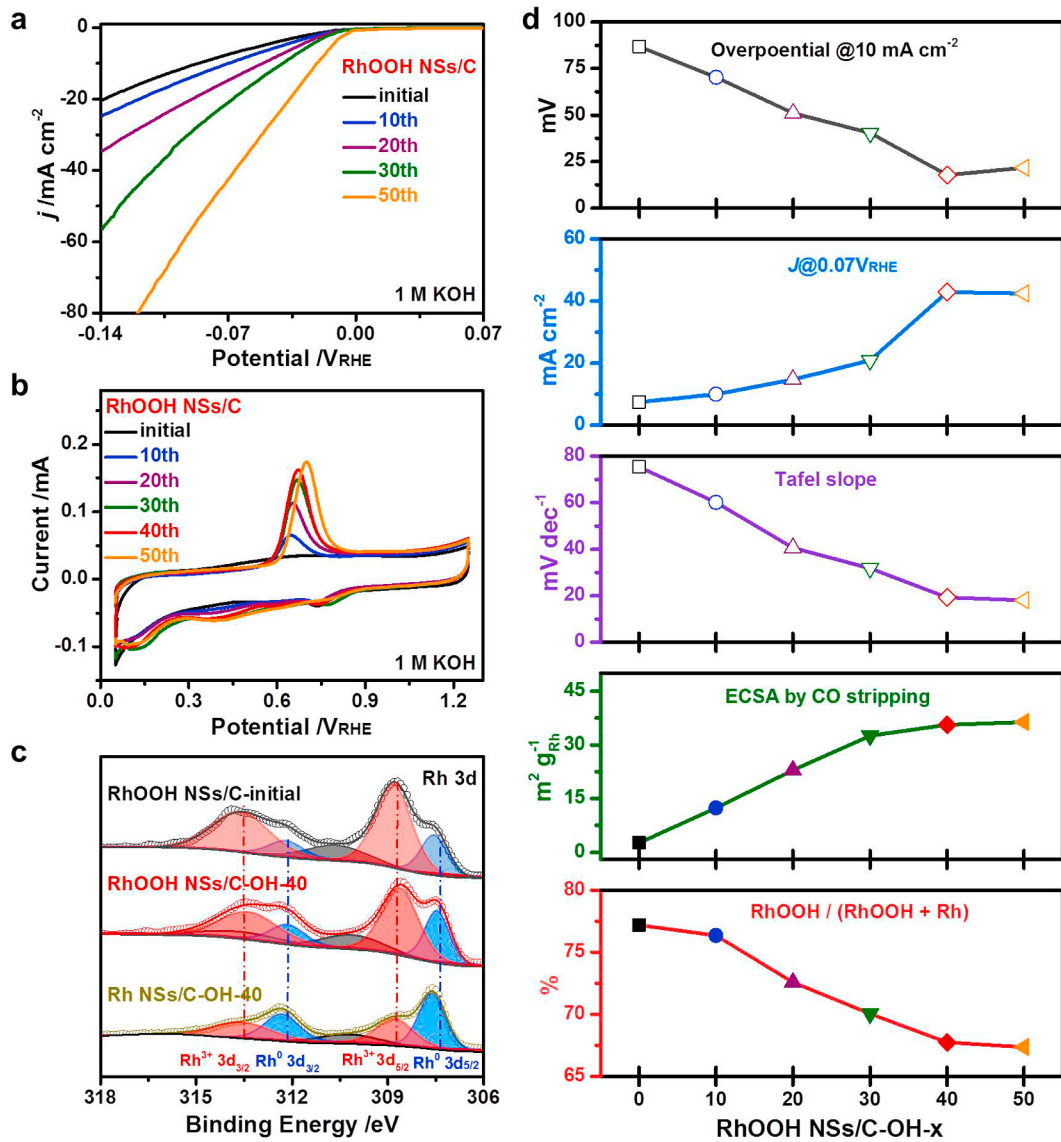


Fig. 3. The effect of CV activation cycles on alkaline HER performance. (a) Polarization curves and (b) CO stripping curves of RhOOH NSs/C after different CV activation cycles in 1 M KOH. (c) Rh 3d XPS spectra of RhOOH NSs/C-initial, RhOOH NSs/C-OH-40, and Rh NSs/C-OH-40. (d) The effects of CV activation cycles 1 M KOH on the overpotential at 10 mA cm^{-2} , current density at 0.07 V , Tafel slope, ECSA calculated by CO stripping and RhOOH/(RhOOH + Rh) ratio.

RhOOH, respectively [40,41]. For Rh_2O_3 -com, the peaks at 533.0 and 529.5 eV were indexed as adsorbed OH species (OH_{ad}), and O_{ox} in Rh_2O_3 , respectively [40,41]. Furthermore, TPR measurements were performed for RhOOH NSs/C and Rh_2O_3 -com. As depicted in Fig. S15c, an intensive H_2 consumption peak appeared at 53°C in the H_2 -TPR curve of RhOOH NSs/C, which corresponded to the reduction peak of RhOOH. In contrast, the H_2 consumption peaks were observed at 73, 102, and 121°C in the TPR curve of Rh_2O_3 -com. Based on these results from XPS, TPR, XRD, TGA and HRTEM measurements, we further confirmed the formation of RhOOH species after calcination. The RhOOH/(RhOOH + Rh) ratio was further calculated by integrating the area of peak in XPS spectra. As shown in Table S3, the RhOOH/(RhOOH + Rh) ratio of RhOOH NSs/C-initial was 77.2%, which gradually decreased to 67.3% when the CV activation cycles were increased to 50. We thus summarized the correlation between RhOOH/(RhOOH + Rh) ratio and HER performance, as displayed in Figs. 3d and S16. The RhOOH/(RhOOH + Rh) ratio-dependent HER performance suggested that strong synergy RhOOH/Rh at the interface, which was *in situ* formed during CV activation process, played a vital role in alkaline HER.

Afterwards, HRTEM measurement was performed on RhOOH NSs/C-

C-OH-40. As shown in Fig. 4, the lattices of 0.223 and 0.216 nm in the HRTEM images of RhOOH NSs/C-OH-40 (Fig. 4a-e), which corresponded to RhOOH (111) facet (Fig. 4f) and metallic Rh (111) facet (Fig. 4g), respectively. No obvious changes of RhOOH/Rh structure were observed for the RhOOH NSs/C-OH-50, suggesting that the slight decrease in HER activity comparing with RhOOH NSs/C-OH-40 was attributed to the different ratios between RhOOH and Rh on the surface (Fig. S17). The above results indicated that RhOOH was gradually reduced into Rh during the CV activation process (Fig. 4h). To further investigate the RhOOH/(RhOOH + Rh) ratio-dependent HER performance, control experiments were performed by activating the RhOOH NSs/C in 0.1 M HClO_4 for 40 cycles (named as RhOOH NSs/C-H-40). Rh 3d XPS spectrum of RhOOH NSs/C-H-40 displayed that the RhOOH/(RhOOH + Rh) ratio was 34.9%, which was obviously lower than that of RhOOH NSs/C-OH-40 (67.7%) (Fig. S18). CO stripping experiment on RhOOH NSs/C-H-40 showed that the onset potential of CO stripping peak largely shifted from $0.56 \text{ V}_{\text{RHE}}$ to $0.61 \text{ V}_{\text{RHE}}$, indicating that the formation of OH_{ad} was strongly suppressed (Fig. S19a). In addition, RhOOH NSs/C-H-40 was used as catalyst for HER in 1 M KOH. It was found that RhOOH NSs/C-H-40 exhibited a much lower HER activity

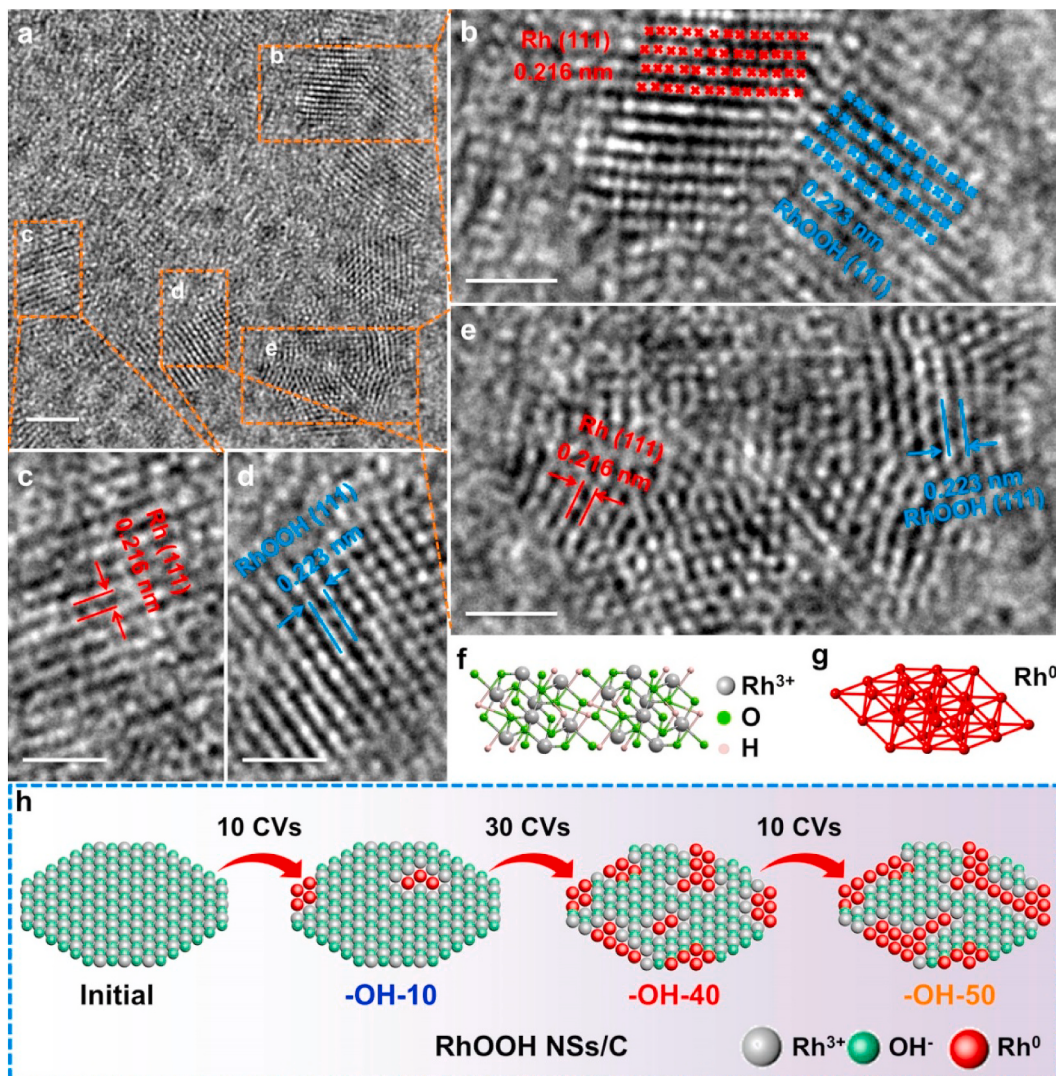


Fig. 4. SATEM image of RhOOH NSs/C-OH-40 and proposed schematic diagram. (a) SATEM image and (b–e) the magnified regions in (a). Local ball-and-stick model of (f) RhOOH and (g) Rh. (h) The proposed schematic diagram for RhOOH NSs/C during the CVs activation in alkaline. The scale bars in (a–e) are 2, 1, 1, 1 and 1 nm, respectively.

than that of RhOOH NSs/C-OH-40 (current density: 22.7 vs. 42.9 mA cm⁻² at 0.07 V_{RHE}) (Fig. S19b), further indicating the significance of strongly synergized RhOOH/Rh interface on alkaline HER. Therefore, the excellent alkaline HER of RhOOH NSs/C-OH-40 with lower overpotential and Tafel slope was attributed to the hetero-interface consisting of RhOOH and Rh. The RhOOH species in the RhOOH/Rh hetero-interface promoted the H₂O dissociation and thereby facilitated the formation of H_{ad} intermediates on the Rh surface, meanwhile, Rh species in the RhOOH/Rh hetero-interface enhanced the H_{ad} desorption to produce H₂. This synergy on the hetero-interface of the metal and metal compounds has been widely studied in the alkaline HER, that is, the so-called “ensemble effect” [42–44].

DFT calculations were carried out to better understand the superior alkaline HER performance (Fig. 5). In DFT calculation, we considered three simulation models, including pure Rh, pure Pt, and Rh(111)-Rh-O interface (to mimic the RhOOH/Rh interface). The atomic structures of these three systems are shown in Fig. 5a. The calculation is on the level of Perdew-Burke-Ernzerhof (PBE) with D3 dispersion correction. The entropy and solvation effect were also included in the calculation (More details about the simulation models and methods are in computational details). In the experiment, it is found that the Tafel slope of Pt is 48.1 mV·dec⁻¹, which indicates an apparent transfer coefficient of 0.48 e⁻ (or

0.5 e⁻ electron transfer). Thus, the kinetic of alkaline HER is controlled by the reaction of water dissociation in Volmer reaction, the first proton-coupled electron transfer reaction [35]. Accordingly, we carried the Climbing-image Nudged Elastic Band (CI-NEB) calculation to investigate the reaction barrier of water dissociation, which was widely employed as a valid descriptor to predict the performance [45,46]. The calculation results were shown in Fig. 5b and Table S4. As shown in Fig. 5b, the energy barrier of water dissociation on Pt is 0.721 eV. Instead, the water dissociation energy barrier of Rh is 0.466 eV, which is much lower than that of Pt, explaining the improved alkaline HER performance on Rh. The introduction of interface on Rh further decreases the water dissociation energy barrier to 0.419 eV. Meanwhile, the free energy difference of partially oxidized Rh is the lowest among the three cases, suggesting that the strong synergy at the interface can significantly enhance HER activity, which is consistent with our experimental observations (Fig. 5b). On the other hand, we also calculated the adsorption energy of the H atom on different surfaces (Fig. 5c). As shown in Table S5, compared to the pure Rh system, the absorption free energy of H atom is slightly reduced after the introduction of interface on Rh. Considering the free energy barriers of different systems (Fig. 5b), we conclude that introduction of interface can strongly improve alkaline HER performance (Fig. 5d), despite that Pt gives the lowest H atom

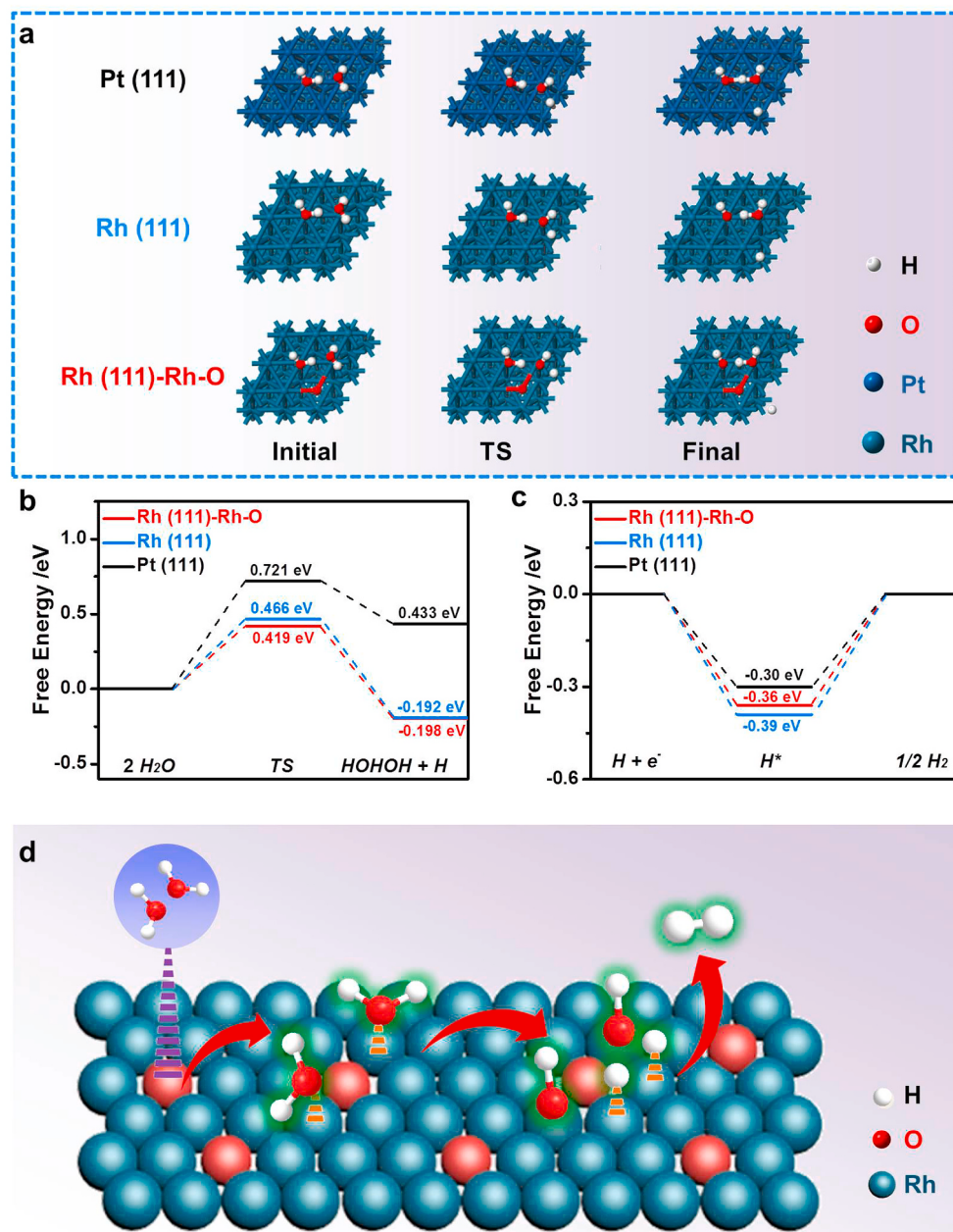


Fig. 5. Theoretical investigation and proposed mechanism for alkaline HER. (a) Configurations of the initial state, transition state (TS), and final state on Pt(111), Rh(111) and Rh(111)-Rh-O interface. (b) Reaction Gibbs free energy diagram for H_2O dissociation and (c) the adsorption energy of the H atom on Pt(111), Rh(111), and Rh(111)-Rh-O interface. (d) Schematic showing the proposed mechanism for alkaline HER on the Rh(111)-Rh-O interface.

adsorption free energy among the three cases. In addition, a new model of RhOOH (P21 space group) (111) surface was selected to mimic the partial reduction of RhOOH. This model consisted of 104 atoms (24 Rh atoms, 56 O atoms, and 24 H atoms). Experimental observations suggested that $\sim 1/3$ Rh³⁺ (32.3%) were reduced into Rh⁰ for RhOOH NSs/C-OH-40 (Table S3). Therefore, half of O and H atoms were removed from the RhOOH structure, and Rh metal was embedded in the RhOOH framework (MER), as depicted in Fig. S20. The MER structure had two possible H adsorption sites, which were labeled as MER-a and MER-b, respectively (Fig. S20). DFT calculations were carried out to investigate the H binding and H_2O binding, which has been widely adopted as the descriptor for HER performance. As shown in Table S6, DFT results indicated that the adsorption free energy of H_2O molecule for Rh/RhOOH-b sites was -0.58 eV, which was much lower than that

for Rh/RhOOH-a site (-0.20 eV). On the other hand, the adsorption free energies of H atom on Rh/RhOOH-a site and Rh/RhOOH-b site were -0.44 and -0.24 eV, respectively. Based on those aforementioned results, we conclude that Rh/RhOOH interface played an important role for improving the alkaline HER performance by weakening the H adsorption and strengthening the H_2O adsorption.

4. Conclusion

In summary, we demonstrated a facile and precise surface engineering of RhOOH NSs for the alkaline HER activity. By altering the cyclic voltammogram cycles in the activation process, the surface structure of RhOOH NSs can be precisely tuned, leading to the formation of strongly synergized RhOOH/Rh interface. As a result, the optimized

RhOOH NSs/C-OH-40, which was activated in 1 M KOH for 40 CV activation cycles, exhibited superior alkaline HER performance alkaline HER performance with overpotential of 18 mV at current density of 10 mA·cm⁻² and Tafel slope of 19.3 mV·dec⁻¹ in 1 M KOH. More importantly, the current density at 0.07 V_{RHE} in 1 M KOH of RhOOH NSs/C-OH-40 was 3.7 times higher than that of commercial Pt/C under the same conditions, being one of the best alkaline HER electrocatalysts reported so far. Mechanism studies and DFT calculations suggested that the strongly synergized RhOOH/Rh interface significantly enhanced the adsorption/dissociation of H₂O to H_{ad} and the desorption of H_{ad} to H₂, leading to the enhanced alkaline HER activity. This work highlights the significance of surface engineering on alkaline HER activity, which may shed new light on the development of efficient catalysts for electrochemical water splitting.

CRediT author statement

X.H. conceived and supervised the research. X.H., S.B., and Y.X. designed the experiments. X.H., S.B., K.C., and Y.X. conducted the experiments and data analysis. T.C. and M.X. performed the theoretical computations and analyzed the theoretical results. X.H., S.B., and Y.X. wrote the paper

Declaration of competing interest

The authors declare that they have no known competing financial interests or personal relationships that could have appeared to influence the work reported in this paper.

Acknowledgment

This work was financially supported by the Ministry of Science and Technology (2016YFA0204100, 2017YFA0208200), the National Natural Science Foundation of China (21571135, 51802206), Young Thousand Talented Program, Jiangsu Province Natural Science Fund for Distinguished Young Scholars (BK20170003), Natural Science Foundation of Jiangsu Province (BK20180846), the Priority Academic Program Development of Jiangsu Higher Education Institutions (PAPD), and the start-up supports from Soochow University.

Appendix A. Supplementary data

Supplementary data to this article can be found online at <https://doi.org/10.1016/j.nanoen.2020.105224>.

References

- [1] M.R. Gao, Y.F. Xu, J. Jiang, S.H. Yu, Chem. Soc. Rev. 42 (2013) 2986–3017.
- [2] J. Baxter, Z. Bian, G. Chen, D. Danielson, M.S. Dresselhaus, A.G. Fedorov, T. S. Fisher, C.W. Jones, E. Maginn, U. Kortshagen, A. Manthiram, A. Nozik, D. R. Rolison, T. Sands, L. Shi, D. Sholl, Y. Wu, Energy Environ. Sci. 2 (2009) 559–588.
- [3] S. Chandrasekaran, L. Yao, L. Deng, C. Bowen, Y. Zhang, S. Chen, Z. Lin, F. Peng, P. Zhang, Chem. Soc. Rev. 48 (2019) 4178–4280.
- [4] L. Li, P. Wang, Q. Shao, X. Huang, Chem. Soc. Rev. (2020), <https://doi.org/10.1039/D0CS00013B>.
- [5] C. Hu, L. Zhang, J. Gong, Energy Environ. Sci. 12 (2019) 2620–2645.
- [6] H. Zhang, P.K. Shen, Chem. Rev. 112 (2012) 2780–2832.
- [7] S. Park, Y. Shao, J. Liu, Y. Wang, Energy Environ. Sci. 5 (2012) 9331–9344.
- [8] Y. Liang, Y. Li, H. Wang, J. Zhou, J. Wang, T. Regier, H. Dai, Nat. Mater. 10 (2011) 780–786.
- [9] A. Vojvodic, J.K. Nørskov, Science 334 (2011) 1355–1356.
- [10] L.A. Stern, L. Feng, F. Song, X. Hu, Energy Environ. Sci. 8 (2015) 2347–2351.
- [11] W. Sheng, M. Myint, J.G. Chen, Y. Yan, Energy Environ. Sci. 6 (2013) 1509–1512.
- [12] P. Wang, X. Zhang, J. Zhang, S. Wan, S. Guo, G. Lu, J. Yao, X. Huang, Nat. Commun. 8 (2017) 14580.
- [13] Y. Zheng, Y. Jiao, A. Vasileff, S.-Z. Qiao, Angew. Chem. Int. Ed. 57 (2018) 7568–7579.
- [14] X. Wu, S. Zhou, Z. Wang, J. Liu, W. Pei, P. Yang, J. Zhao, J. Qiu, Adv. Energy Mater. 9 (2019) 1901333.
- [15] C. Wan, Y.N. Regmi, B.M. Leonard, Angew. Chem. Int. Ed. 53 (2014) 6407–6410.
- [16] J. Greeley, T.F. Jaramillo, J. Bonde, I.B. Chorkendorff, J.K. Nørskov, Nat. Mater. 5 (2006) 909–913.
- [17] Y. Wu, X. Liu, D. Han, X. Song, L. Shi, Y. Song, S. Niu, Y. Xie, J. Cai, S. Wu, J. Kang, J. Zhou, Z. Chen, X. Zheng, X. Xiao, G. Wang, Nat. Commun. 9 (2018) 1425.
- [18] R. Subbaraman, D. Tripkovic, D. Strmcnik, K.-C. Chang, M. Uchimura, A. P. Paulikas, V. Stamenkovic, N.M. Markovic, Science 334 (2011) 1256–1260.
- [19] R. Subbaraman, D. Tripkovic, K.C. Chang, D. Strmcnik, A.P. Paulikas, P. Hirunsit, M. Chan, J. Greeley, V. Stamenkovic, N.M. Markovic, Nat. Mater. 11 (2012) 550–557.
- [20] N. Danilovic, R. Subbaraman, D. Strmcnik, K.C. Chang, A.P. Paulikas, V. R. Stamenkovic, N.M. Markovic, Angew. Chem. Int. Ed. 51 (2012) 12495–12498.
- [21] W. Sheng, Z. Zhuang, M. Gao, J. Zheng, J.G. Chen, Y. Yan, Nat. Commun. 6 (2015) 5848.
- [22] J. Zheng, W. Sheng, Z. Zhuang, B. Xu, Y. Yan, Sci. Adv. 2 (2016), e1501602.
- [23] I. Ledezma-Yanez, W.D.Z. Wallace, P. Sebastián-Pascual, V. Climent, J.M. Feliu, M. T.M. Koper, Nat. Energy 2 (2017) 17031.
- [24] E. Liu, J. Li, L. Jiao, H.T.T. Doan, Z. Liu, Z. Zhao, Y. Huang, K.M. Abraham, S. Mukerjee, Q. Jia, J. Am. Chem. Soc. 141 (2019) 3232–3239.
- [25] G. Kresse, J. Hafner, Phys. Rev. B 47 (1993) 558–561.
- [26] G. Kresse, J. Furthmüller, Comput. Mater. Sci. 6 (1996) 15–50.
- [27] G. Kresse, J. Furthmüller, Phys. Rev. B 54 (1996) 11169–11186.
- [28] J.P. Perdew, K. Burke, M. Ernzerhof, Phys. Rev. Lett. 77 (1996) 3865–3868.
- [29] S. Grimme, J. Antony, S. Ehrlich, H. Krieg, J. Chem. Phys. 132 (2010) 154104.
- [30] P.E. Blöchl, Phys. Rev. B 50 (1994) 17953–17979.
- [31] G. Kresse, D. Joubert, Phys. Rev. B 59 (1999) 1758–1775.
- [32] Z. Weng-Sieh, R. Gronsky, A.T. Bell, J. Catal. 170 (1997) 62–74.
- [33] N. Zhang, Q. Shao, Y. Pi, J. Guo, X. Huang, Chem. Mater. 29 (2017) 5009–5015.
- [34] M. Peuckert, Surf. Sci. 141 (1984) 500–514.
- [35] J. Durs, A. Siebel, C. Simon, F. Hasché, J. Herranz, H.A. Gasteiger, Energy Environ. Sci. 7 (2014) 2255–2260.
- [36] L. Zhuang, J. Jin, H.D. Abruna, J. Am. Chem. Soc. 129 (2007) 11033–11035.
- [37] X. Huang, D. Teschner, M. Dimitrakopoulou, A. Fedorov, B. Frank, R. Krahnert, F. Rosowski, H. Kaiser, S. Schunk, C. Kuretschka, R. Schlgl, M.-G. Willinger, A. Trunschke, Angew. Chem. Int. Ed. 58 (2019) 8709–8713.
- [38] L. Zhang, M.R. Ball, Y. Liu, T.F. Kuech, G.W. Huber, M. Mavrikakis, I. Hermans, J. A. Dumesic, ACS Catal. 9 (2019) 1810–1819.
- [39] K. Liu, W. Wang, P. Guo, J. Ye, Y. Wang, P. Li, Z. Lyu, Y. Geng, M. Liu, S. Xie, Adv. Funct. Mater. 29 (2018) 1806300.
- [40] L.S. Kibis, A.I. Stadnichenko, S.V. Koscheev, V.I. Zaikovskii, A.I. Boronin, J. Phys. Chem. C 120 (2016) 19142–19150.
- [41] A.A. Tolia, R.J. Smiley, W.N. Delgass, C.G. Takoudis, M.J. Weaver, J. Catal. 150 (1994) 56–70.
- [42] T. Kwon, M. Jun, J. Joo, K. Lee, J. Mater. Chem. A 7 (2019) 5090–5110.
- [43] M.K. Kundu, R. Mishra, T. Bhowmik, S. Barman, J. Mater. Chem. A 6 (2018) 23531–23541.
- [44] Z. Li, Y. Feng, Y.-L. Liang, C.-Q. Cheng, C.-K. Dong, H. Liu, X.-W. Du, Adv. Mater. 32 (2020) 1908521.
- [45] G. Henkelman, H. Jónsson, J. Chem. Phys. 113 (2000) 9978–9985.
- [46] G. Henkelman, B.P. Uberuaga, H. Jónsson, J. Chem. Phys. 113 (2000) 9901–9904.